Mehrnoosh Afshar, Jay Carriere, Tyler Meyer, Ronald Sloboda, Siraj Husain, Nawaid Usmani, Mahdi Tavakoli, Optimal Design of a Novel Spherical Scissor Linkage Remote Center of Motion Mechanism for Medical Robotics, IEEE/RSJ International Conference on Intelligent Robots and Systems, Las Vegas, USA, 2020.

Optimal Design of a Novel Spherical Scissor Linkage Remote Center of Motion Mechanism for Medical Robotics

Mehrnoosh Afshar[1], Jay Carriere[1], Tyler Meyer[2], Ron Sloboda[3], Siraj Husain[2], Nawaid Usmani[3], and Mahdi Tavakoli[1]

***Abstract*— In this paper, a new remote center of motion (RCM) mechanism is presented whose end-effector is able to move through an entire hemisphere. In general, minimally invasive surgery (MIS) applications, an elliptic cone workspace with vertex angles of 60° and 90° gives the surgeon enough freedom to operate. Therefore, the majority of the developed RCM mechanisms have such a cone as the workspace. However, there are still situations in which a larger workspace is required, like the breast ultrasound scanning application in which the RCM mechanisms should be able to move over a hemisphere to do the breast scanning. The proposed RCM mechanism is developed based upon a spherical scissor linkage and benefits from the high stiffness characteristics of parallel structures while eliminating the common problem of linkage collision in parallel structures. It has two rotational degrees of freedom that are decoupled from each other. The Jacobian and the stiffness of the mechanism while considering the bending of the links is calculated through the virtual joints method (VJM). The kinemato-static equations and the methodology for calculating stiffness are described in detail. The optimal arc angle of the mechanism's links is found using a multi-objective genetic algorithm optimization. A prototype of the mechanism is built and forward kinematic of the proposed mechanism is examined experimentally. The experiments indicate that the proposed mechanism is able to provide a hemisphere as its workspace while the RCM point of the mechanism is fixed in the space.**

I. INTRODUCTION

The employment of robots and mechanisms in the medical application such as surgeries and therapies offers benefits including high accuracy, repeatability, and remote accessibility. One of the specific applications where robots are used in medical procedures is ultrasound imaging with robots. In standard practice, the ultrasound probe is manipulated by a physician. The experience and knowledge of the physician directly influence the ultrasound image quality. Physicians find it difficult to hold an ultrasound transducer for a long period of time in a fixed position and apply a proper perpendicular force to the patient's body in order to obtain a high-quality ultrasound image. Therefore, one of our motivations is to design a system to support the human-assisted ultrasound examination to avoid musculoskeletal injuries prevalent among ultrasound technicians.

In this paper we propose the design of a spherical RCM mechanism to be used as a breast ultrasound scanning probe holder. An ultrasound probe can be attached to the proposed spherical RCM mechanism, where the hemispherical workspace of the RCM will allow for straightforward scanning of a patient's breast at any desired angle. The main design requirements for the spherical RCM mechanism are as follows:

1) The workspace of the proposed mechanism should cover a full hemisphere.
2) The proposed mechanism should not have any internal singularities within the workspace.
3) For the sake of simplicity in manipulation and control, degrees of freedom of the mechanism should be decoupled.
4) The total stiffness of the mechanism should be high in order to guarantee ultrasound positioning accuracy in the presence of robot/tissue contact.

To achieve these requirements, an RCM mechanism which is built upon a spherical scissors linkage will be devised. The suggested mechanism has two decoupled rotational DoFs and an RCM located outside the mechanism. The proposed RCM mechanism can provide a complete hemisphere workspace without any singularities within the workspace. This mechanism can be motorized and has the advantage that the motors stay in a fixed position on the mechanism base (i.e. the motors do not move with the links).

Studies demonstrate that the conical workspace, provided by an RCM, with vertex angles of 60° and 90° degrees suffices for most procedures in minimally invasive surgery (MIS) [1]. The positioning of the RCM mechanism is critical when a limited workspace is provided, and a user has to move and adjust the position of the RCM mechanism when a surgeon needs to operate from multiple directions around the patient's body. An RCM mechanism with a large workspace, like hemisphere/sphere, is able to mitigate the necessity for RCM repositioning during the operation. Therefore, another motivation for this paper is to design an RCM mechanism that has a larger workspace, covering an entire hemisphere.

The paper is organized as follows: Background material will be reviewed in Section II. Mechanism design and kinematics will be presented in Sections III-A and III-B. An analytic stiffness derivation and the isotropy will be discussed in Sections IV and V, respectively. Further analysis and design optimization will be elaborated in Section VI. Prototype design and experimental evaluation will be presented in Section VII, and the paper will be completed by a conclusion in Section VIII.

This research was supported by the Canada Foundation for Innovation (CFI) under grant LOF 28241; the Alberta Innovation and Advanced Education Ministry under Small Equipment Grant RCP-12-021; the Natural Sciences and Engineering Research Council (NSERC) of Canada under the Collaborative Health Research Projects (CHRP) Grant #316170

[1]Mehrnoosh Afshar, Jay Carriere, and Mahdi Tavakoli (Corresponding Author) are with the Department of Electrical and Computer Engineering, University of Alberta, AB, Canada T6G 1H9. afsharbo@ualberta.ca, jtcarrie@ualberta.ca, mahdi.tavakoli@ualberta.ca

[2]Tyler Meyer and Siraj Husain are with the Division of Radiation Oncology, Tom Baker Cancer Centre, 331 29th Street NW, Calgary, Alberta T2N 4N2. tyler.meyer@albertahealthservices.ca, siraj.husain@albertahealthservices.ca.

[3]Ron Sloboda and Nawaid Usmani are with the Department of Oncology, Cross Cancer Institute, 11560 University Avenue, Edmonton, AB, Canada, T6G 1Z2. nawaid.usmani@albertahealthservices.ca, ron.sloboda@albertahealthservices.ca.

II. Background

Generally, RCM mechanisms can be classified into several basic categories based on their kinematics [2]. The eight kinematic categories include isocenters, parallelograms, circular tracking arcs, synchronous belt transmission mechanisms, spherical linkages, parallel manipulators, compliant mechanisms, and passive RCMs [2]. Among those categories, parallelograms and parallel spherical linkages have gained the most popularity in the literature.

Most of the studies on RCM mechanism have focused on MIS robots, in which designed laparoscopic instruments need to undergo spherical motions pivoted at the point of entry into the patient's body [3]. For ultrasound imaging assistance, RCM mechanisms are typically employed as a dexterous robotic wrists, where the tip of the ultrasound probe is placed at the RCM point of the mechanism; however, when an RCM mechanism is intended to be used as a probe holder for ultrasound breast examination, the probe need to have a spherical motion centered at the breast center. Many works have been conducted to utilize robotic platforms for breast examination [4], however, an RCM mechanism has never been developed specifically for this application.

Many of the MIS robots have been built upon primary parallelogram mechanisms including Neurobot [5], and BlueDRAGON [6]. The authors in [7] proposed a rotating pantograph, generating a conical workspace for ultrasound scanning. A three DoFs movable robot, which works based on a parallel pantograph and a gimbal mechanism and should be mounted on the patient's body, is designed in [8]. Three degrees of freedom in this robot are coupled together and in order to reach a specific configuration, all joints should move together in a controlled manner. Additional configurations of parallelogram such as dual triangular-mechanism [9] and a combination of a dual parallelogram and Peaucellier-Lipkin straight-line linkage [10] have been developed. Parallelogram-based RCM mechanisms have the drawback of linkage collision and workspace-boundary singularity. To avoid collision between the two transverse bars of the parallelogram, the bars should be mounted far enough from each other, which increases the RCM mechanism size.

Two other categories of RCM mechanisms, spherical and circular tracking arc mechanisms, benefit from the geometric features of sphere and circle, respectively. Circular tracking-based RCM mechanisms have the ability to provide relatively large workspace and high mechanism stiffness. A limitation of circular tracking-based RCM mechanisms is that the arced links must be very large in order to maintain an acceptable distance between the desired RCM location and robot links to guarantee that robot does not confine the surgeon's workspace during the operation. An RCM mechanism comprising of circular guides linked together in a serial arrangement was constructed in [11]. The bulkiness of the system is one of its main drawbacks.

In spherical mechanisms, linkages are spherical sections with a common rotation center being the RCM point. Spherical RCM mechanisms exist in both serial and parallel configurations. Cures [12] and Raven-II [13] are RCM robots that adopted the concept of serial spherical linkages in their structure. A serial spherical linkage by mounting a two-revolute joint spherical mechanism on a circular guide is developed in [1]. The arc angle of each spherical link in [1] was derived through an optimization problem with the aim of maximizing the manipulability index while preserving the compactness of the system. In this work, the parallel configuration of the mechanism was also investigated. In-vivo suturing and tissue manipulation experiments were used to assess the rate of collision problem in a serial and parallel configuration; higher collisions were reported for the parallel configuration [1].

One concern that exists for spherical serial manipulators is their low stiffness; however, parallel manipulators have shown superiority in stiffness and precision in comparison to their serial counterparts. A parallel spherical mechanism consisting of three "limbs," with each limbs consisting of two spherical links in series (3RR), is devised in [14]. A three-limb spherical RCM mechanism utilizing prismatic joints (3PRP) was developed in [15]. The complicated structure of these mechanisms, which consists of at least three limbs, leads to linkage interferences and an internal singularity if the limbs are not sufficiently long. Additionally, these 3-limb mechanisms cannot cover an entire hemisphere. A 2-DoF spherical parallel mechanism in [16] can provide the standard cone workspace without interference and singularity in a compact and simple form. Again, however, the workspace of this mechanism is limited to a cone. Our proposed mechanism, which can be categorized as parallel spherical mechanisms, is able to sufficiently provide a hemispherical workspace without internal singularity and with the required stiffness for medical purposes.

III. Mechanism Design and Kinematics

In this section, first, the main conceptual design and embodiment of the mechanism will be represented. Secondly, the kinematics of the proposed spherical mechanism, in which the individual link compliance is taken into account, is introduced.

A. Conceptual Design

In spherical mechanisms, all of the device's links are curved and are constrained to move on a spherical surface, defined the radius of the links. In this paper, the number of links and their arc angles are designed in order to cover a hemisphere. Fig. 1a and Fig. 1b show the mechanism at its starting and final configurations, respectively. Considering geometric constraints between the links in the scissor mechanism, the end-effector is confined to move along a circle, at the intersection between the hemispherical workspace and the mechanism's plane shown in Fig. 1b. Therefore, the mechanism can traverse a circular path in a 2D plane with only one control input, which controls the relative angle between the first and second links. In order to eliminate the "dead length" of the conventional scissor mechanism, we designed the mechanism to consist of various stages, which are arranged in a cascade manner. Each link is associated with a spherical section with the spherical radius differing between links; as illustrated in Fig. 1. In this paper, the number of links and their arc angles are designed in order to cover a hemisphere. Fig. 1a and Fig. 1b show the mechanism at its starting and final configurations, respectively. While it is also possible to optimize for the radii of the arced links, we have chosen them based on the size of the ultrasound probe.

B. Forward Kinematics

One of the most important performance indicators of manipulators is their mechanical stiffness. The mechanical stiffness of

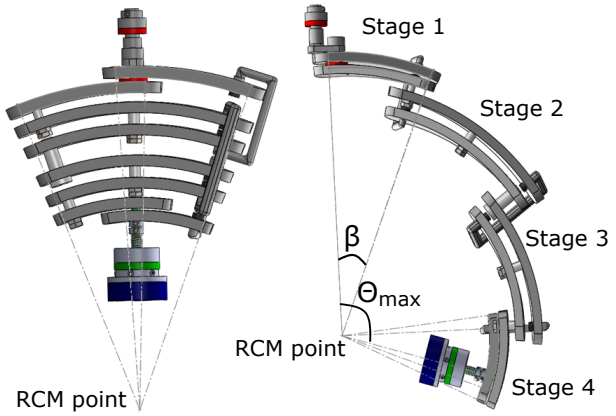

(a) Initial configuration (b) Final configuration

Fig. 1: Model of the mechanism with four stages.

the manipulator defines the amount of deflection with respect to external force/torque exerted to the end-effector. The higher the mechanical stiffness of a manipulator, the lower its positioning error under load. Low positioning error is crucial in medical robotics; hence, the mechanical stiffness of the robot should be high. To model the manipulator stiffness, we will use the Virtual Joint Method (VJM), which is regarded as a computationally efficient approach and is generally used in the pre-design stage.

In VJM, elastic deformations of links and joints are modeled using virtual springs located at joints. The axis of the virtual spring at each joint is normal to the link's bending plane. To simplify VJM implementation and derivation of the governing kinematics for the proposed mechanism, a distinction will be made between 1) actuated joints, 2) virtual joints and 3) passive joints.

1) Actuated joints: For the proposed mechanism, we only need 2 DoFs (two actuated joints) to cover our desired hemispherical workspace. The first actuated joint, Θ_1, controls the relative angle between the two curved links in stage one of the mechanism, which provides a circular planar motion for the mechanism. The second actuated joint, Θ_0, rotates the entire mechanism along the common axis of the mechanism and provide 3D motion of the mechanism (Fig. 2). Activation for Θ_1 and Θ_0 can be provided either by motors placed at those joints, or by a user moving the end-effector on a sphere. [1]
2) Virtual joints: Each flexible links is substituted by a rigid link, which is connected to the previous link by a torsion spring. The joints parameters corresponding to virtual springs are called virtual joints.
3) Passive joints: All other joints in the mechanism structure, which are driven by actuated joints are called passive joints.

The forward kinematics will be derived based on the Denavit-Hartenberg (DH) convention. The DH parameters of the actuated and virtual joints, as generalized coordinates, contribute to the forward kinematics equations. The passive joints parameters can be calculated based on actuated and virtual joint parameters using analytical equations. Following the conventional approach for the forward kinematic analysis of closed-loop mechanisms, the mechanism is separated into two branches, where the right and left branches are depicted in Fig. 2. There is a repetitive pattern for DH parameters between stages of the mechanism. The DH parameters for the first stage of the left branch links are summarized in Table I, and the generic DH parameters for the other stages of the left branch links are summarized in Table II. Due to the symmetry of the mechanism, the angles θ_i and α_i of the right branch are equal to the negative of those for the left branch, and the lengths a_i and d_i are equal for both branches. The link frames and virtual frames of the links associated with the left branch and the first stage of the mechanism are illustrated in Fig. 3. In Fig. 3, red frames represent the real link frames (similar to those for the usual rigid mechanism), and blue frames indicate the virtual frames associated with each virtual spring, which are shown. For more illustration about θ_i parameters in Table I, each θ_i, which is the angle between x_{i-1} and x_i along z_i, is shown in detail in Fig. 3.

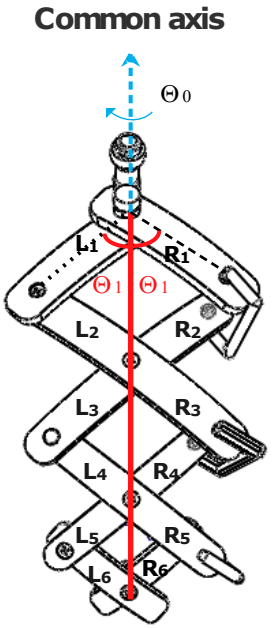

Fig. 2: Partitioning and links labeling of left/right branches in the mechanism.

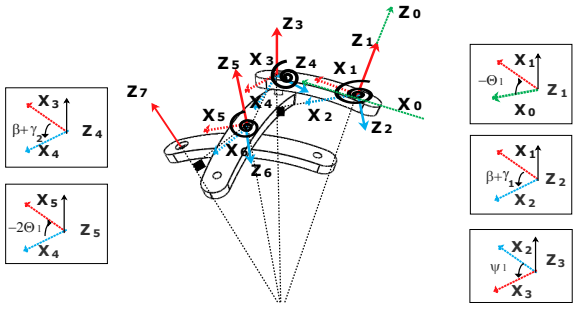

Fig. 3: Description of left branch's links in terms of Denavit–Hartenberg parameters.

[1] https://youtu.be/wxHEEwwRnGU

TABLE I: Denavit-Hartenberg for the links of the first stage of the mechanism from the left branch.

Links	θ_i	α_i	a_i	d_i
1	Θ_0	0	0	0
2	$-\Theta_1$	0	0	0
3	$\beta+\gamma_1$	$\frac{-\pi}{2}$	0	0
4	ψ_1	$\frac{\pi}{2}$	$R_3 sin(\beta)$	$R_3-R_3 cos(\beta)$
5	$\beta+\gamma_2$	$\frac{-\pi}{2}$	0	0
6	$-2\Theta_1$	$\frac{\pi}{2}$	$R_5 sin(\beta)$	$R_5-R_5 cos(\beta)$

In Table I, R_3 and R_5 are the distances between the RCM point and the centers of the 3_{th} and 5_{th} links, respectively. β is the arc angle that is common to all links. ψ_1 is the rotation angle (Fig. 3), which is a passive angle and should be found based on Θ_1,β ,γ_1, and γ_2. In Table II, s is the stage number of the mechanism. To

TABLE II: Denavit-Hartenberg for the links of the other stages of the mechanism from the left branch

Links	θ_i	α_i	a_i	d_i
$4(s-1)+3$	$\beta+\gamma_{2(s-1)+1}$	$\frac{-\pi}{2}$	0	0
$4(s-1)+4$	ψ_s	$\frac{\pi}{2}$	$R_{4(s-1)+3} sin(\beta)$	$R_{4(s-1)+3}-R_{4(s-1)+3} cos(\beta)$
$4(s-1)+5$	$\beta+\gamma_{2(s-1)+2}$	$\frac{-\pi}{2}$	0	0
$4(s-1)+6$	$-2\Theta_1$	$\frac{\pi}{2}$	$R_{4(s-1)+5} sin(\beta)$	$R_{4(s-1)+5}-R_{4(s-1)+5} cos(\beta)$

find ψ_i in each stage, we will consider the standard homogeneous transformation for the left branch ${}^L T_n$ and the right branch ${}^R T_n$ of the mechanism separately where,

$$\begin{aligned} {}^R T_n^0(\theta) &= {}^R T_1^0(\theta_1)\, {}^R T_2^1(\theta_2) \ldots {}^R T_n^{n-1}(\theta_n) \\ &= \left[\begin{array}{c|c} {}^R R_n^0 & {}^R P_n^0 \\ \hline \mathbf{0}^T & 1 \end{array}\right] \end{aligned} \tag{1}$$

$$\begin{aligned} {}^L T_n^0(\theta) &= {}^L T_1^0(\theta_1)\, {}^L T_2^1(\theta_2) \ldots {}^L T_n^{n-1}(\theta_n) \\ &= \left[\begin{array}{c|c} {}^L R_n^0 & {}^L P_n^0 \\ \hline \mathbf{0}^T & 1 \end{array}\right] \end{aligned} \tag{2}$$

Given that the end-effector position in both the left and right branches in each stage must be equal, i.e. ${}^R P_n^0 \equiv {}^L P_n^0$, an analytic formula to derive ψ_i can be found as

$$\psi_i = \cos^{-1}\left(\frac{a_{1,i}\sqrt{a_{1,i}^2+a_{2,i}^2-a_{3,i}^2}+a_{2,i}a_{3,i}}{a_{1,i}^2+a_{2,i}^2}\right) \tag{3}$$

where

$$a_{1,i} = \cot(\Theta_1),\ a_{2,i} = \cos(\beta+\gamma_i),\ a_{3,i} = -\cot(\beta+\gamma_{i+1})\sin(\beta+\gamma_i) \tag{4}$$

such that, γ_i is the DH parameter for virtual links (i.e. virtual springs) in each stage and β is arc angle of links.

IV. Mechanical Stiffness

In order to derive the stiffness equation, we need to analytically develop kinemato-static set of equations. The nonlinear kinematic equation is given by

$$p = f(\theta,\gamma) \tag{5}$$

Here, vector p represents the position/orientation of end-effector in the Cartesian space. Vectors θ and γ contain the actuated and the virtual joint coordinates, respectively. From (5), we can get

$$\delta p = J_\theta \delta\theta + J_\gamma \delta\gamma \tag{6}$$

where $\delta\gamma$ is the virtual angular displacement due to the bending of links from a nominal static position and $\delta\theta$ is the virtual angular displacement of the actuated joints. J_θ and J_γ are the kinematic Jacobin with respect to θ and γ coordinates, respectively.

A kinemato-static model can be developed based on the principle of virtual work in equilibrium static condition. The equation

$$F^T \delta p - \tau_\gamma^T \delta\gamma - \tau_\theta^T \delta\theta = 0 \tag{7}$$

explains the static equilibrium equations extracted from the virtual work principle. Here, F is the external force exerted to end-effector. τ_γ is the reaction torque in the γ coordinates and τ_θ is the actuator's torques in the θ coordinates. Putting (6) into (7) results in

$$\begin{aligned} F^T J_\gamma &= \tau_\gamma^T \\ F^T J_\theta &= \tau_\theta^T \end{aligned} \tag{8}$$

An auxiliary torque-angular displacement equation, from Hooke's law for virtual coordinates, γ, governs the virtual coordinates:

$$\tau_\gamma = K_\gamma \delta\gamma \tag{9}$$

K_γ is the stiffness matrix in the virtual joint coordinates. Given an external force F and the desired end-effector position p, the mechanism configuration (θ,γ) must be derived from the following system of nonlinear equations:

$$\begin{aligned} p &= f(\vec{\theta},\gamma) \\ J_\gamma^T F &= K_\gamma \delta\gamma \end{aligned} \tag{10}$$

In (10), the first equation describes nonlinear kinematic equation and the second equation describes the relationship between the applied force to the virtual joints with the angular deflections of virtual joints based on Hooke's law. As an inverse-kinematics problem, (10) is required to be solved numerically. Despite the non-linearity of (10), the linear stiffness matrix is much more desirable for design purposes. Therefore, we perform the linearization for the model around θ coordinates. As we intend to extract the part of end-effector displacement that is resulted from the link's deflection, we assume that $\delta\theta = 0$. Then

$$J_\gamma^T F = K_\gamma \delta\gamma = K_\gamma J_\gamma^T \delta\gamma \tag{11}$$

rearrangement of (11) results in

$$F = J_\gamma K_\gamma J_\gamma^T \delta\gamma \tag{12}$$

where

$$K_c = J_\gamma K_\gamma J_\gamma^T \tag{13}$$

represents the Cartesian stiffness of the manipulator (K_c). K_γ, is the equivalent stiffness of a curved flexible beam which is

subjected to the bending force at its free end while the other end is clamped, is given by [17]

$$\Delta = \frac{F_i R_i^3}{E_i I_i}\left(\frac{1}{2}\phi_i - \frac{1}{2}\sin\phi_i\cos\phi_i\right) \tag{14}$$

where Δ is the deflection of beam's free end due to bending force, F_i, and ϕ_i and R_i are radius and arc angle of the curved beam (Fig. 4). Our objective is to replace flexible curved links with a torsional spring mounted on the base of a rigid one. The torsional stiffness of virtual spring is what leads to the same tip deflection for the beam under the equivalent torque. Based on the work-energy principle, the amount of bending force work is equal to the deflection energy stored in the torsional spring. Therefore, the equivalent stiffness is given by

$$F_i\Delta = \frac{1}{2}K_{\gamma_i}(\Gamma_i)^2 \tag{15}$$

such that K_{γ_i} is the equivalent torsional stiffness of the beam. Γ_i, which is deflection angle, can be estimated by (based on Fig. 4).

$$\Gamma_i = \frac{\Delta}{L_i} = \frac{\Delta}{R_i\frac{\sin(\varphi_i)}{\cos(\frac{1}{2}\varphi_i)}} \tag{16}$$

Therefore, K_{γ_i} can be calculated as

$$K_{\gamma_i} = \frac{4E_iI_i\sin(\varphi_i)^2}{R_i\cos(\frac{1}{2}\varphi_i)^2(\varphi_i - \sin(\varphi_i))\cos(\varphi_i)} \tag{17}$$

where E_i is the modulus of elasticity and I_i is the moment of inertia. There are various approaches for deriving algebraic characteristic of the stiffness matrix, such as trace and eigenvalue, in order to be used as the stiffness index. In this paper, given that the probe applies force along the radial direction, the stiffness in the radial direction is much more important than the stiffness in other directions. At each configuration the total Cartesian stiffness matrix calculated by (13) should be rotated and represented based on the frame coordinate of the last revolute joint frame coordinate. Finally, one diagonal element of the stiffness matrix, which is in the direction of the radial axis of the sphere, is adopted as the mechanism's stiffness index in the optimization problem.

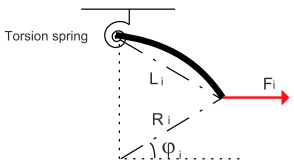

Fig. 4: Curved beam diagram.

V. Isotropy Index

A Jacobian matrix relates the change of actuated joint angular/linear displacement to the angular/linear displacement of the end-effector. In (6), the Cartesian displacement of the end-effector depends on the displacement of the actuated joints and virtual joints. To put it differently, the total Jacobian of a flexible mechanism depends on both the kinematic configuration and the value of external wrench applied to the mechanism. We will define an extra static equation,

$$S(F,\theta,\gamma) = J_\gamma^T F - K\gamma \tag{18}$$

such that the relationship between $\delta\gamma$ and $\delta\theta$ can be derived. Noting that the external force F and Hooke's law forces $K\gamma$ are balanced, we know that $S(F,\theta,\gamma) = 0$. By taking the derivative of $S(F,\theta,\gamma)$, i.e,

$$\frac{\partial S}{\partial\theta}\delta\theta + \frac{\partial S}{\partial\gamma}\delta\gamma = 0, \tag{19}$$

we can find the net Jacobian by putting (19) into (6), resulting in

$$\vec{p} = \left[J_\theta + J_\gamma\left(\frac{\partial S}{\partial\gamma}\right)^{-1}\frac{\partial S}{\partial\theta}\right]\delta\theta = J_{net}\delta\theta \tag{20}$$

If the mechanism is considered to be fully rigid then $J_\gamma = 0$ and $J_{net} = J_\theta$. Generally, the Jacobian transforms a hyper-plane in the joint space into an ellipsoid which is referred to the manipulability ellipsoid in the Cartesian space. The closer to a unit sphere the manipulability ellipsoid is, the lower the level of error in control positioning of the manipulator's end-effector. The condition number of the Jacobian can be used as a performance index that characterizes the amount of error amplification from the joint space to the Cartesian space, ranging from 1 to infinity. The manipulator is called isotropic when the condition number is equal to 1, which means the manipulator has identical movement performance in all directions. Usually, the manipulability index, which is the inverse of the condition number and ranging from 0 to 1, is used to evaluate the mechanical performance through the workspace. Given that the manipulability index value depends on the manipulator configuration, a global condition index (GCI) introduced by [18] will be used to calculate the kinematic performance. GCI is simply an average of isotropy index over the workspace.

$$\text{GCI} = \frac{\int_W(\frac{1}{\kappa})dW}{\int_W dW} \tag{21}$$

where W is the manipulator's reachable space and $\kappa = \frac{\sigma_{max}}{\sigma_{min}}$ is the condition number of the Jacobian matrix. σ_{max} and σ_{min} are maximum and minimum singular value of the Jacobian matrix, respectively. In case of internal singularity, the determinant of the Jacobian matrix is zero and the condition number of the Jacobian matrix reaches to infinity (i.e. a large number).

VI. Further Analysis and Design Optimization

The maximum reachable angle in mechanism's workspace, Θ_{max}, is found from the arc angle of links, β, and the number of links in each branch (left/right) of a mechanism, N (see Fig. 1).

$$\Theta_{max} = \beta N \tag{22}$$

thus, given a desirable Θ_{max}, there are many options to choose a pair of β and N. However, the isotropy and the stiffness of the mechanism vary based on the choice of this pair. To cover a large range of workspace, either β or N should increase. Fig. 5 and Fig. 6 depict the mechanism's minimum stiffness and GCI index variation, respectively, across various possible pairs of N and β. Fig. 5 indicates that given a fixed workspace line, a structure that has a larger number of links (a larger N) and a smaller β is stiffer than a structure with a fewer number of links and a larger β; in fact, the parallel structure of the mechanism causes this. As shown in Fig. 6, different combinations of N and β affect the isotropy index as well. If N is increased, with β decreasing in proportion to N such that Θ_{max} remains constant, the isotropy index will remain constant or grows slightly. If β expands, while N remaining fixed,

the isotropy index will initially increase to some maximum value and then decrease. To plot the stiffness and the isotropy index map, we choose the modulus of elasticity of aluminum, $E = 200Gpa$, and curved links with a rectangular section of size $1 \times 3cm^2$.

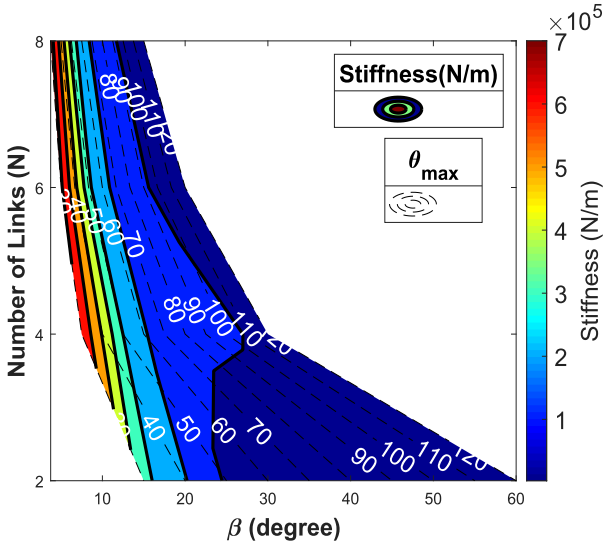

Fig. 5: Minimum stiffness map in the β-N plane.

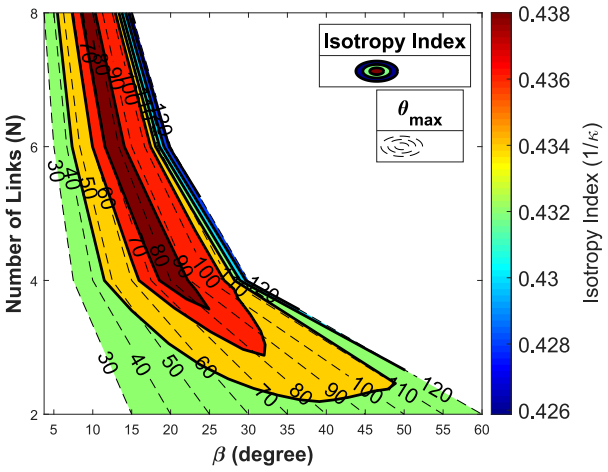

Fig. 6: Global Isotropy index (GCI) map in the β-N plane.

Consequently, we are faced with an optimization problem of finding an optimal β, as a design variable, in order to enhance the stiffness and the isotropy of the mechanism simultaneously. In this paper, β is constrained to be between 10° and 45°. To find β, we faced with a multi-objective optimization problem as

$$\max_{\beta} \{K_c(\beta), GCI(\beta)\}$$
$$\text{constraints} = \begin{cases} N\beta = \frac{\pi}{2} \\ 10^\circ \ll \beta \ll 45^\circ \end{cases} \quad (23)$$

Generally, in multi-objective optimization problems a set of solutions called the Pareto frontier, P_f, are attained instead of one particular optimum solution. The Pareto frontier is a border that its points cannot dominate each other in terms of optimization objectives. Each point selected from the Pareto frontier, $p_i = \langle GCI_i, K_i \rangle \in P_f$, can be used as an optimum solution based on the user's preference. In this paper, we select the one that has higher stiffness among the Pareto frontier's points, such that $\langle GCI_i, K_i \rangle_{optimal} = \max_{p_i}(K_i)$.

A genetic algorithm (GA) is used to perform the optimization problem.Due to the stochastic nature of the GA, the results that are obtained from each run differ from each other. In Table III, the mean and standard deviation of 10 optimization results are shown. The stiffness and the isotropy index of the mechanism through the entire hemispherical workspace are depicted in Fig. 7a and Fig. 7b, respectively, for selected $\beta = 18^\circ$. The isotropy index equal or close to 0, represents the singularity of the mechanism within the workspace. The minimum isotropy index of the mechanism across the workspace is 0.0382, which is associated with the boundaries of the workspace. Such a minimum isotropy index for boundaries is common among all mechanisms. Considering the isotropy index distribution of the mechanism in Fig. 7b, being singularity free of the mechanism can be approved.

TABLE III: The optimal parameters averaged over 10 runs.

	Mean	Standard Deviation
β	18.21°	0.39°
GCI Index	0.45	1.75e−4
Stiffness (N/m)	1.99e+5	0.07

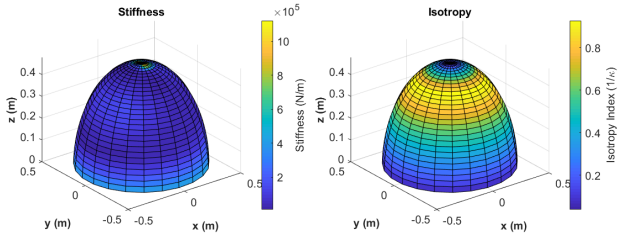

(a) Stiffness across the workspace (b) Isotropy across the workspace

Fig. 7: Stiffness and isotropy map.

VII. Prototype Design and Experimental Evaluation

A prototype of the proposed mechanism with curved angle of $\beta = 18^\circ$ was built (Fig. 8). The Fig. 8a ,and Fig. 8b describe the initial configuration of the mechanism when links are completely closed and the final configuration in which the mechanism completely cover a 90° arc in space, respectively.

To experimentally validate the spherical workspace and forward kinematic derivation of the proposed RCM device an electromagnetic tracker was attached to the center of the end effector of the fabricated prototype spherical RCM mechanism (shown in Fig. 8). The RCM mechanism was tested by changing the angle Θ_1 (see Fig. 2) in discrete steps such that $\Theta_1 \in \{45^\circ, 50^\circ, ...80^\circ\}$. For each value of Θ_1 that was tested, the device was rotated about Θ_0, the first degree-of-freedom, within the range $\Theta_0 \in [-\pi/8 : \pi/8]$ while the end effector position data was measured by the electromagnetic tracker. For the fabricated prototype device, the distance from the RCM point to measured end effector position should ideally be 0.24 m throughout the entire workspace, and was experimentally measured to be 0.246 ± 0.004 m. Fig. 9 shows the results of the work space validation graphically.

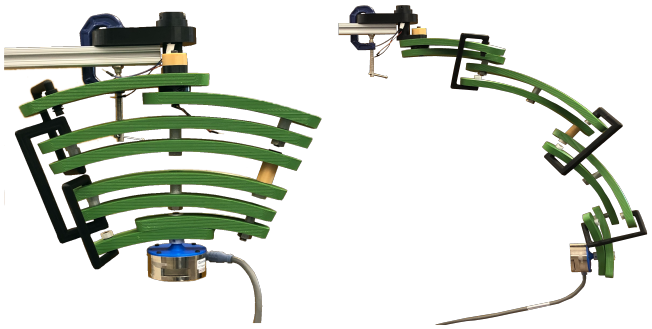

(a) Initial configuration (b) Final configuration

Fig. 8: Prototype of the proposed spherical RCM mechanism.

The contour value in Fig. 9 describes the difference between the real position of the prototype's end-effector and the ideal position from forward kinematic calculation. These results indicate that the workspace of the fabricated prototype device closely matches the designed workspace and that the RCM mechanism functions as expected also the correctness of the forward kinematic calculation is verified. For these tests, an Aurora electromagnetic tracker with a Planar 20-20 V2 Field Generator (NDI Europe GmbH, Radolfzell, Germany) was used. The ranges of the values for Θ_0 and Θ_1 were chosen to ensure the end-effector electromagnetic tracker remained within the tracking volume provided by the planar field generator.

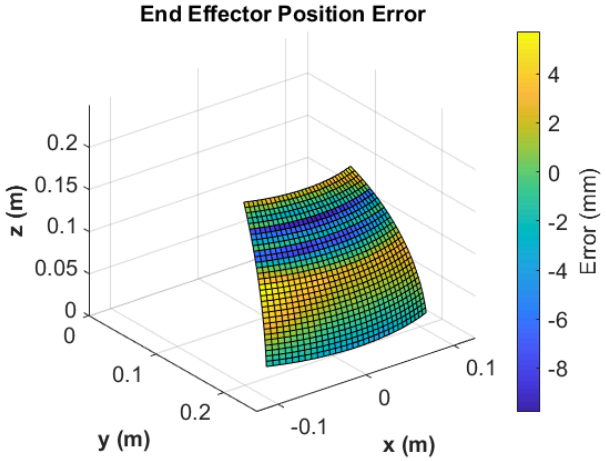

Fig. 9: Comparison of measured end-effector position of prototype and theoretical end-effector position.

VIII. Conclusion

In this paper, the kinemato-static equation for a novel spherical RCM mechanism with an arbitrary number of stages was introduced. A closed-form solution for the forward kinematics of the mechanism was derived. Presented kinematic equations took the links flexibility into account. A relationship for the mechanism stiffness was derived. The stiffness, the isotropy index and singularity of the mechanism were investigated throughout the entire hemispherical workspace. The result of the isotropy analysis indicates that the mechanism is singularity free within this workspace. The optimal links arc angle for a hemispherical workspace was found by considering the isotropy index and the stiffness as the mechanism performance index.

References

[1] M. J. Lum, J. Rosen, M. N. Sinanan, and B. Hannaford, "Kinematic optimization of a spherical mechanism for a minimally invasive surgical robot," in *IEEE International Conference on Robotics and Automation, 2004. Proceedings. ICRA'04. 2004*, vol. 1. IEEE, 2004, pp. 829–834.

[2] C.-H. Kuo and J. S. Dai, "Robotics for minimally invasive surgery: a historical review from the perspective of kinematics," in *International symposium on history of machines and mechanisms*. Springer, 2009, pp. 337–354.

[3] M. Tavakoli, R. Patel, and M. Moallem, "A haptic interface for computer-integrated endoscopic surgery and training," *Virtual Reality (Special Issue on Haptic Interfaces and Applications)*, vol. 9, no. 2-3, pp. 160–176, 2006.

[4] J. Carriere, J. Fong, T. Meyer, R. Sloboda, S. Husain, N. Usmani, and M. Tavakoli, "An admittance-controlled robotic assistant for semi-autonomous breast ultrasound scanning," in *2019 International Symposium on Medical Robotics (ISMR)*, April 2019, pp. 1–7.

[5] B. Davies, S. Starkie, S. J. Harris, E. Agterhuis, V. Paul, and L. M. Auer, "Neurobot: a special-purpose robot for neurosurgery," in *Proceedings 2000 ICRA. Millennium Conference. IEEE International Conference on Robotics and Automation. Symposia Proceedings (Cat. No. 00CH37065)*, vol. 4. IEEE, 2000, pp. 4103–4108.

[6] J. Rosen, J. D. Brown, L. Chang, M. Barreca, M. Sinanan, and B. Hannaford, "The bluedragon-a system for measuring the kinematics and dynamics of minimally invasive surgical tools in-vivo," in *Proceedings 2002 IEEE International Conference on Robotics and Automation (Cat. No. 02CH37292)*, vol. 2. IEEE, 2002, pp. 1876–1881.

[7] S. E. Salcudean, W. H. Zhu, P. Abolmaesumi, S. Bachmann, and P. D. Lawrence, "A robot system for medical ultrasound," in *Robotics Research*. Springer, 2000, pp. 195–202.

[8] K. Masuda, E. Kimura, N. Tateishi, and K. Ishihara, "Three dimensional motion mechanism of ultrasound probe and its application for tele-echography system," in *Proceedings 2001 IEEE/RSJ International Conference on Intelligent Robots and Systems. Expanding the Societal Role of Robotics in the the Next Millennium (Cat. No. 01CH37180)*, vol. 2. IEEE, 2001, pp. 1112–1116.

[9] S. T. Liu, L. Harewood, B. Chen, and C. Chen, "A skeletal prototype of surgical arm based on dual-triangular mechanism," *Journal of Mechanisms and Robotics*, vol. 8, no. 4, p. 041015, 2016.

[10] G. Chen, J. Wang, and H. Wang, "A new type of planar two degree-of-freedom remote center-of-motion mechanism inspired by the peaucellier–lipkin straight-line linkage," *Journal of Mechanical Design*, vol. 141, no. 1, p. 015001, 2019.

[11] M. Mitsuishi, S. Warisawa, T. Tsuda, T. Higuchi, N. Koizumi, H. Hashizume, and K. Fujiwara, "Remote ultrasound diagnostic system," in *Proceedings 2001 ICRA. IEEE International Conference on Robotics and Automation (Cat. No. 01CH37164)*, vol. 2. IEEE, 2001, pp. 1567–1574.

[12] S.-K. Kim, W.-H. Shin, S.-Y. Ko, J. Kim, and D.-S. Kwon, "Design of a compact 5-dof surgical robot of a spherical mechanism: Cures," in *2008 IEEE/ASME International Conference on Advanced Intelligent Mechatronics*. IEEE, 2008, pp. 990–995.

[13] B. Hannaford, J. Rosen, D. W. Friedman, H. King, P. Roan, L. Cheng, D. Glozman, J. Ma, S. N. Kosari, and L. White, "Raven-ii: an open platform for surgical robotics research," *IEEE Transactions on Biomedical Engineering*, vol. 60, no. 4, pp. 954–959, 2012.

[14] T. Li and S. Payandeh, "Design of spherical parallel mechanisms for application to laparoscopic surgery," *Robotica*, vol. 20, no. 2, pp. 133–138, 2002.

[15] S. Bai, "Optimum design of spherical parallel manipulators for a prescribed workspace," *Mechanism and Machine Theory*, vol. 45, no. 2, pp. 200–211, 2010.

[16] W.-a. Cao, S.-j. Xu, K. Rao, and T. Ding, "Kinematic design of a novel two degree-of-freedom parallel mechanism for minimally invasive surgery," *Journal of Mechanical Design*, vol. 141, no. 10, p. 104501, 2019.

[17] W. C. Young, R. G. Budynas *et al.*, *Roark's formulas for stress and strain*, 2002, vol. 7.

[18] C. Gosselin, *Kinematic analysis, optimization and programming of parallel robotic manipulators*. McGill University Montréal, Canada, 1988.